

# Odd-Parity Chiral Magnons in Collinear Antiferromagnetic Multiferroics: Symmetry Classification and Ferroelectric Switching

Quanchao Du,<sup>1,\*</sup> Zhenlong Zhang,<sup>1,\*</sup> Yuanjun Jin,<sup>2</sup> Rui Li,<sup>1</sup> Haibo Xie,<sup>1</sup>  
Jinlian Lu,<sup>3</sup> Zhe Wang,<sup>1</sup> Zhijun Jiang,<sup>1,†</sup> Lei Zhang,<sup>1</sup> and Jinyang Ni<sup>1,‡</sup>

<sup>1</sup>*Ministry of Education Key Laboratory for Nonequilibrium*

*Synthesis and Modulation of Condensed Matter,*

*Shaanxi Province Key Laboratory of Advanced Functional Materials and Mesoscopic Physics,*

*School of Physics, Xi'an Jiaotong University, Xi'an 710049, China*

<sup>2</sup>*Guangdong Basic Research Center of Excellence for*

*Structure and Fundamental Interactions of Matter,*

*Guangdong Provincial Key Laboratory of Quantum Engineering and Quantum Materials,*

*School of Physics, South China Normal University, Guangzhou 510006, China*

<sup>3</sup>*Department of Physics, Yancheng Institute of Technology, Yancheng, Jiangsu 224051, China*

## Abstract

The coupling between ferroelectrics and magnetism presents a promising avenue for low-dissipation spintronic devices. However, such couplings remain rare, and the direct realization of magnetic order driven by ferroelectric switching in insulators continues to pose a significant challenge. Here, we identify a class of collinear antiferromagnetic multiferroics in which intra-sublattice Dzyaloshinskii-Moriya interaction (DMI) induces odd-parity chiral magnons that are reversible via ferroelectric switching. Leveraging the charge-neutral nature of magnons, such multiferroics enable non-volatile ferroelectric control over magnon spin splitting, Hall transport, and spin polarization in antiferromagnetic insulators. Remarkably, magnetic group analysis and spin wave calculations reveal that the chiral splitting adopts three planar odd-parity forms,  $f$ -wave,  $p$ -wave, and fully-gapped types, with an intriguing Néel vector dependence. Furthermore, density functional theory calculations validate various material candidates, ranging from two-dimensional to bulk systems. Our work provides new insights into the realization of odd-parity chiral magnons in collinear antiferromagnets and opens new avenues for magnetoelectric coupling mechanisms in multiferroics.

---

\* These authors contributed equally to this work.

† zjjiang@xjtu.edu.cn

‡ jyini@xjtu.edu.cn

## I. INTRODUCTION

In modern spintronics, achieving non-volatile magnetic control is a central objective; accordingly, ferroelectric-based manipulation, owing to its high energy efficiency, is widely regarded as an ideal approach for state switching [1–4]. In multiferroics, the coexistence of ferroelectric and magnetic orders theoretically allows for the direct manipulation of magnetic orders through ferroelectric polarization [5–11]. However, practical implementation of such control faces significant challenges. On the one hand, most multiferroics are intrinsically antiferromagnetic with weak magnetoelectric (ME) coupling, rendering magnetic response induced by ferroelectric switching too weak to be effectively detected, as exemplified by Type-I multiferroics [5, 12, 13]. On the other hand, in Type-II multiferroics, magnetically induced polarization is limited by weak spiral order and low polarization [8, 14, 15]. Consequently, achieving strong magnetoelectric coupling while maintaining observable magnetic order parameters continues to be a major trade-off.

Recent breakthroughs in unconventional magnets have introduced a new paradigm for multiferroics through the coupling of ferroelectric order with spin degrees of freedom [16–26]. Unlike ferromagnets and antiferromagnets, unconventional magnets exploit the intrinsic interplay between spin and spatial symmetries to achieve spin splitting in the absence of spin-orbit coupling [27–29]. This gives rise to a unique duality, which combines the compensated magnetic order of antiferromagnets with the spin-polarized properties of ferromagnets [30–32]. Consequently, spatial symmetry has emerged as a key design degree of freedom for achieving direct ferroelectric spin coupling, where momentum-dependent spin splitting serves as an effective order parameter for magnetic responses induced by ferroelectric switching [19–26]. Despite these advancements, the reliance of spin-polarized currents on a finite Fermi surface, coupled with the inevitable spin dissipation arising from Joule heating, remains a fundamental obstacle to technological implementation.

To address this challenge, this work establishes a coupling between ferroelectric order and magnon chiral splitting in collinear antiferromagnetic multiferroics, providing an effective way to overcome the above bottleneck. By leveraging the chiral degrees of freedom of antiferromagnetic magnons combined with the ferroelectric switching, such multiferroics enable the non-volatile control of long-range spin angular momentum transport in insulators without Joule heating [33, 34]. Symmetry analysis reveals that this chiral splitting originates from the intra-sublattice Dzyaloshinskii-Moriya interaction (DMI) driven by the ferroelectric mode, and it can be further

classified into odd-parity  $p$ -wave,  $f$ -wave and fully-gapped types. Notably, such odd-parity splitting gives rise to pronounced and ferroelectrically switchable Hall responses and spin polarization. We further enumerate the possible magnetic space groups associated with this phenomenon and validate material candidates in both two-dimensional (2D) and bulk multiferroics using density functional theory (DFT) calculations.

## II. RESULTS

### A. Model for $f$ - and $p$ -wave magnons

We first elucidate how DMI drives the  $f$ - and  $p$ -wave chiral splitting of magnons in A-type layered antiferromagnets while preserving spin conservation. For concreteness, we consider a layered triangular antiferromagnet with AB stacking, which exhibits a honeycomb Néel order from the top view, as shown in Fig. 1(a). The corresponding effective spin model can be expressed as :

$$\hat{\mathcal{H}} = \hat{\mathcal{H}}_1 + \hat{\mathcal{H}}_2, \quad (1)$$

where  $\hat{\mathcal{H}}_1$  describes the nearest neighbor (NN) Heisenberg interlayer antiferromagnetic spin exchange, given as

$$\hat{\mathcal{H}}_1 = \mathcal{J}_1 \sum_{\langle i,j \rangle} \mathcal{S}_{i,\uparrow} \cdot \mathcal{S}_{j,\downarrow}. \quad (2)$$

$\hat{\mathcal{H}}_2$  accounts for the NN intralayer Heisenberg spin exchange and the Dzyaloshinskii-Moriya interaction (DMI) [35, 36], given by

$$\hat{\mathcal{H}}_2 = \sum_{\langle i,j \rangle, \sigma} \mathcal{J}_{2,\sigma} (\mathcal{S}_{i,\sigma} \cdot \mathcal{S}_{j,\sigma}) + \mathcal{D}_z \sum_{\langle i,j \rangle, \sigma} \boldsymbol{\nu}_{ij} \cdot (\mathcal{S}_{i,\sigma} \times \mathcal{S}_{j,\sigma}). \quad (3)$$

Here,  $\sigma = \uparrow, \downarrow$ ,  $\mathcal{J}_{2,\sigma} < 0$  ensures that the layer antiferromagnet stabilizes a collinear Néel order. For DMI, as shown in Figs. 1 (b) and (e), the sign of  $\boldsymbol{\nu}$  between sublattices is opposite [37–39] when  $\mathcal{P}$  is preserved, whereas it becomes identical when  $\mathcal{P}$  is broken. Note that in the latter case, the opposite spins are connected by the vertical mirror  $\mathcal{M}$  and time reversal  $\mathcal{T}$  symmetry, which preserves the sublattice symmetry [40, 41],  $\mathcal{S}_\uparrow = \mathcal{S}_\downarrow = \mathcal{S}$  and  $\mathcal{J}_{2,\uparrow} = \mathcal{J}_{2,\downarrow} = \mathcal{J}_2$ .

After Holstein-Primakoff and linear spin wave (LSW) approximation [37, 42], the quartic magnon Hamiltonian can be expressed in the spinor basis  $\psi_{\mathbf{k}}^\dagger = (\hat{a}_{\mathbf{k}}^\dagger, \hat{b}_{-\mathbf{k}}, \hat{a}_{-\mathbf{k}}, \hat{b}_{\mathbf{k}}^\dagger)$  as  $\hat{\mathcal{H}} =$

$\sum_{\mathbf{k}} \psi_{\mathbf{k}}^\dagger \hat{\mathcal{H}}_{\mathbf{k}} \psi_{\mathbf{k}}$ . For the layered antiferromagnets with  $\mathcal{P}$  preserved,  $\hat{\mathcal{H}}_{\mathbf{k}}$  can be expressed as :

$$\frac{\hat{\mathcal{H}}_{\mathbf{k}}}{S} = (\lambda + \mathcal{J}_{2\mathbf{k}})I + \begin{pmatrix} f_{\mathbf{k}} & \gamma_{\mathbf{k}} & 0 & 0 \\ \gamma_{\mathbf{k}}^\dagger & -f_{\mathbf{k}} & 0 & 0 \\ 0 & 0 & -f_{\mathbf{k}} & \gamma_{\mathbf{k}}^\dagger \\ 0 & 0 & \gamma_{\mathbf{k}} & f_{\mathbf{k}} \end{pmatrix}, \quad (4)$$

where  $\gamma_{\mathbf{k}} = \mathcal{J}_1 \sum_i \exp(i\mathbf{k} \cdot \boldsymbol{\delta}_i)$ ,  $f_{\mathbf{k}} = \mathcal{D}_z \sum_{i \in \text{odd}} 2\sin(\mathbf{k} \cdot \boldsymbol{\mu}_i)$ ,  $\mathcal{J}_{2\mathbf{k}} = \mathcal{J}_2 \sum_{i \in \text{odd}} 2\cos(\mathbf{k} \cdot \boldsymbol{\mu}_i) - 6$ ,  $\lambda = 3\mathcal{J}_1$  and  $I$  denotes the identity matrix,  $\boldsymbol{\delta}_i$  and  $\boldsymbol{\mu}_i$  refer to the nearest neighbor interlayer and intralayer linking vectors for the layered antiferromagnets, respectively. By employing the Bogoliubov transformation [43–45], the eigenvalues can be obtained :

$$\epsilon_{\alpha,\beta}(\mathbf{k}) = \sqrt{(\lambda + \mathcal{J}_{2\mathbf{k}})^2 - |\gamma_{\mathbf{k}}|^2} + f_{\mathbf{k}}. \quad (5)$$

Clearly, as shown in Fig. 1(c), the  $\alpha$  and  $\beta$  magnon modes are degenerate throughout the Brillouin zone, and the emergence of  $\mathcal{D}_z$  only induces nonreciprocity between in-plane  $\mathbf{k}$  and  $-\mathbf{k}$  points [37, 45–48].

By contrast, when  $\mathcal{P}$  is broken, as illustrated in Fig. 1(d), the corresponding magnon Hamiltonian on the spinor basis  $\psi_{\mathbf{k}}^\dagger$  takes the form :

$$\frac{\hat{\mathcal{H}}_{\mathbf{k}}}{S} = (\lambda + \mathcal{J}_{2\mathbf{k}})I + \begin{pmatrix} f_{\mathbf{k}} & \gamma_{\mathbf{k}} & 0 & 0 \\ \gamma_{\mathbf{k}}^\dagger & f_{\mathbf{k}} & 0 & 0 \\ 0 & 0 & -f_{\mathbf{k}} & \gamma_{\mathbf{k}}^\dagger \\ 0 & 0 & \gamma_{\mathbf{k}} & -f_{\mathbf{k}} \end{pmatrix}, \quad (6)$$

Similarly, Eq. (6) can be diagonalized by using the Bogoliubov transformation, where the eigenvalues are given as :

$$\epsilon_{\alpha,\beta} = \sqrt{(\lambda + \mathcal{J}_{2\mathbf{k}} \pm f_{\mathbf{k}})^2 - |\gamma_{\mathbf{k}}|^2}. \quad (7)$$

Obviously, the introduction of  $\mathcal{D}_z$  can lift the degeneracy of  $\alpha$  and  $\beta$  modes, resulting in the spin-momentum locking band splitting. The magnon bands remain degenerate along the  $\mathbf{k}_z$  direction, as well as along the  $\Gamma$  to M path (and its symmetry-equivalent directions) within each constant- $\mathbf{k}_z$  plane. Along these paths,  $f_{\mathbf{k}} = 0$ , rendering magnon bands effectively equivalent to the  $\mathcal{D}_z$ . Consequently, as shown in Fig. 2(a), the isoenergy contours at  $\mathbf{k}_z = 0$  demonstrate a characteristic planar  $f$ -wave splitting magnon bands. The maximum magnon band splitting occurs at the K point, with a value of approximately  $6\sqrt{3}\mathcal{D}_z$  [49]. Notably, the magnon Hamiltonian of Eq. (6) remains

TABLE 1. The symmetry-allowed magnetic space groups for odd-parity chiral magnons in A-type antiferromagnets. The rotation axis is along the  $z$  direction. For high-symmetry point groups  $6mm$ ,  $6$ ,  $4mm$ , and  $4$ , the Néel vectors are along the  $z$  axis. For  $mm2$ , the Néel vector can be either in-plane ( $x/y$ ) or out-of-plane ( $z$ ), as indicated in parentheses. The symmetry allowed magnon transport and material candidates are also listed.

Point groups	$6mm, 6$ ( $f$ -wave)	$4mm, 4$ ( $p$ -wave)	$mm2$ ( $p$ -wave)	$mm2$ ( $xy$ / fully-gapped)
Magnetic groups	$P6cc, P6'_3m'c, P6'_3, P6'_3cm'$ ,	$PA'_2, PA'm'm, PA_2nm, PA'_2nm',$ $PA'_2cm', PA'_2c'm, P4cc, P4nc,$ $PA'n'c', PA'_2m'c, P4_2bc,$ $PA'_2b'c, PA'_2bc', PA'_2$	$Pcc2, Pma2, Pnc2,$ $Pba2, Pnn2, Ccc2,$ $Abm2, Aba2$	$Pmm2, Pmc2_1, Pma2, Pnc2,$ $Pmn2_1, Cmc2_1, Ama2$
Magnon transport	$\kappa_{xy} \checkmark, \alpha_{xx} \times, \chi_{zx} \times$ $\alpha_{xy} \checkmark, \alpha_{yy} \times, \chi_{zy} \times$	$\kappa_{xy} \times, \alpha_{xx} \times, \chi_{zx} \times$ $\alpha_{xy} \times, \alpha_{yy} \times, \chi_{zy} \checkmark$	$\kappa_{xy} \times, \alpha_{xx} \times, \chi_{zx} \checkmark$ $\alpha_{xy} \times, \alpha_{yy} \times, \chi_{zy} \checkmark$	
Candidates	$w$ -CoS, $w$ -CoSe, LuMnO <sub>3</sub>	K <sub>3</sub> Cr <sub>2</sub> F <sub>7</sub> , Sr <sub>2</sub> MnO <sub>2</sub> F, VSI <sub>2</sub> , VSBr <sub>2</sub>	$w$ -MnSe, $w$ -MnS $w$ -CoO, VOBr <sub>2</sub>	

block diagonal, the  $z$  component spin angular momentum  $s_z$  is conserved; hence the chiral splitting  $\alpha$  and  $\beta$  modes carry opposite  $s_z$ , with chirality  $\mp 1$ , respectively [37, 38, 45].

The above results can be naturally extended to layered orthorhombic antiferromagnets. As shown in Figs. 2(c) and (f), the corresponding magnon bands exhibit planar  $p$ -wave splitting upon introduction of the intralayer DMI ( $\mathcal{P}$  broken), with the crossing band nodes coupling to the lattice symmetry. For layered antiferromagnets with  $\mathcal{C}_4$  rotation symmetry (square lattice), the maximum splitting path occurs along the  $\Gamma$  to M path, while the two-fold degeneracy persists along the  $\Gamma$  to M' path. Upon further symmetry reduction to  $\mathcal{C}_2$  symmetry (rectangular lattice), the maximal splitting shifts to the  $\Gamma$  to X, whereas the bands remain degenerate along the momentum path parallel to the  $y$  axis. Additionally, unlike the  $f$ -wave chiral magnons, the DMI-induced  $p$ -wave splitting shifts the band minimum away from the  $\Gamma$  point to two symmetric points in its vicinity, resulting in a Rashba-like dispersion[50, 51]. In addition, unlike the nonrelativistic odd-parity magnons in nonlinear magnets [52], the odd-parity magnons considered here, including  $p$ - and  $f$ -wave types, retain spin conservation.

Another key feature is the DMI-driven reversal of the odd-parity chiral splitting, as shown in Fig. 2. Since the sign of the DMI is intimately coupled to the ferroelectric polarization, ferroelectric switching provides an efficient means to manipulate odd-parity chiral magnons in layered collinear antiferromagnetic multiferroics. Through group-theoretical analysis, we systematically identify the

polar magnetic point groups compatible with these symmetry requirements. In particular, within the  $6mm$  magnetic point group, the vertical mirror symmetry enforces the symmetry relation between opposite-spin sublattices. As a result, the  $f$ -wave odd-parity chiral splitting arises entirely from the DMI and simultaneously exhibits ferroelectric switchability. We further identify the orthorhombic polar antiferromagnetic point groups capable of hosting  $p$ -wave odd-parity chiral magnons, as summarized in Tab. 1.

### B. Spin transport in $f$ - and $p$ -wave magnons

Polarized magnon bands can generate a finite spin current and lead to spin accumulation when a temperature gradient is applied. For transverse spin currents carried by magnons, their emergence typically requires a finite Berry curvature, corresponding to the imaginary part of the quantum geometric tensor of Bloch wavefunctions [53]. Accordingly, it naturally vanishes in orthorhombic antiferromagnetic magnons with  $p$ -wave, where the magnon Hamiltonian can be represented entirely in a real form. In contrast, a nonzero magnon Berry curvature can arise in hexagonal antiferromagnetic magnons with  $f$ -wave. Given that only the intra-sublattice DMI is considered, and magnons exhibit the planar splitting feature, the  $z$  component Berry curvature  $\Omega^z$  plays a dominant role. It should be emphasized that under the  $\mathcal{P}$  preserving, the  $\Omega^z$  is independent with DMI and satisfies the valley symmetry, i.e.,  $\Omega^z(\mathbf{k}) = -\Omega^z(-\mathbf{k})$  [37, 54], as depicted in Fig. S2(a) [49]. In this case, DMI merely induces nonreciprocity in the magnon bands [45], while the magnon Hall effect vanishes, and only the magnon Nernst response still exists [37–39].

When  $\mathcal{P}$  is broken, the magnon Berry curvature of Eq. (6) becomes dependent on the  $\mathcal{D}_z$  and can be expressed as :

$$\begin{aligned} \Omega_{\alpha,\beta}^z(\mathbf{k}) = \mp \frac{1}{2\epsilon'_0{}^3} & \left[ (3\mathcal{J}_1 + f_{\mathbf{k}} + \mathcal{J}_{2\mathbf{k}}) (\nabla \text{Re } \gamma_{\mathbf{k}} \times \nabla \text{Im } \gamma_{\mathbf{k}}) \right. \\ & \left. + \text{Im } \gamma_{\mathbf{k}} (\nabla (f_{\mathbf{k}} + \mathcal{J}_{2\mathbf{k}}) \times \nabla \text{Re } \gamma_{\mathbf{k}}) + \text{Re } \gamma_{\mathbf{k}} (\nabla \text{Im } \gamma_{\mathbf{k}} \times \nabla (f_{\mathbf{k}} + \mathcal{J}_{2\mathbf{k}})) \right], \end{aligned} \quad (8)$$

where  $\epsilon'_0 = \sqrt{(\lambda + \mathcal{J}_{2\mathbf{k}} + f_{\mathbf{k}})^2 - |\gamma_{\mathbf{k}}|^2}$ . It is noteworthy that magnon Berry curvature is primarily governed by  $\mathcal{J}_1$  and  $\mathcal{D}_z$ , while  $\mathcal{J}_{2\mathbf{k}}$  merely modifies the overall range of magnon Berry curvature, which can be omitted in the following discussion. Notably, as shown in Figs. 3(a) and S2(b) [49], the emergence of  $\mathcal{D}_z$  breaks the valley symmetry of Berry curvature, i.e.,  $\Omega^z(\mathbf{k}) \neq -\Omega^z(-\mathbf{k})$ , which significantly shifts their values near the K and K' points. Furthermore, reversing DMI direction can flip the sign of Berry curvature. The giant chiral splitting and the asymmetric Berry curvature

both gives rise to anomalous Hall transport [55, 56]. The  $z$  component Berry curvature can drive transverse magnon Hall response upon applying the temperature gradient, where the temperature-dependent Hall conductivity  $\kappa_{xy}$  is shown in Fig. 3(b). Clearly, it demonstrates that DMI generates a robust magnon Hall current, with its sign reversibly switched by reversing the DMI, thereby confirming the ferroelectric switching behavior.

In addition to Berry-curvature-driven magnon transport, band splitting can in principle generate longitudinal spin currents, such as the magnon Seebeck effect [57, 58]. However, the Seebeck effect is intrinsically forbidden due to the odd-parity relation of  $f$ -wave and  $p$ -wave chiral magnons,  $s_z(\mathbf{k}) = -s_z(-\mathbf{k})$ . For spin accumulation driven by the Edelstein effect [52, 59], magnons should exhibit asymmetric spin occupation, which requires spin conservation to be broken. As discussed above, easy-axis Néel order preserves spin angular momentum; therefore, easy-plane magnetic anisotropy is generally required to lift this constraint.

### C. Fully-gapped magnons and Edelstein effect

Upon introducing easy-plane anisotropy, the momentum magnon Hamiltonian of layered honeycomb antiferromagnet is modified as follow :

$$\frac{\hat{\mathcal{H}}_{\mathbf{k}}}{S} = (\lambda + \mathcal{J}_{2\mathbf{k}})I + \begin{pmatrix} f_{\mathbf{k}} & \gamma_{\mathbf{k}} & \mathcal{K}_x & 0 \\ \gamma_{\mathbf{k}}^\dagger & f_{\mathbf{k}} & 0 & \mathcal{K}_x \\ \mathcal{K}_x & 0 & -f_{\mathbf{k}} & \gamma_{\mathbf{k}}^\dagger \\ 0 & \mathcal{K}_x & \gamma_{\mathbf{k}} & -f_{\mathbf{k}} \end{pmatrix}, \quad (9)$$

where  $\lambda$  is modified as  $3\mathcal{J}_1 + \mathcal{K}_x$  with  $\mathcal{K}_x > 0$ . Compared to Eq. (6), the emergence of easy-plane anisotropy  $\mathcal{K}_x$  leads to the Hamiltonian not being block diagonal, thereby breaking spin conservation and three-fold rotation symmetry. By employing Bogoliubov transformation, the resulting magnon bands are obtained as shown in the Fig. 4(a), which demonstrates that easy-plane anisotropy additionally lifts the degeneracy at the M and  $\Gamma$  points. Meanwhile, the spin-momentum texture of magnons preserves its odd-parity character and remains reversible under ferroelectric switching. Distinct from the  $f$ -wave and  $p$ -wave chiral splittings discussed above, this odd-parity chiral splitting exhibits a fully gapped character. Based on the above symmetry analysis, we further identify and summarize the magnetic point groups capable of hosting such a fully-gapped phase, as listed in Tab. 1.

The odd-parity spin-momentum locking ensures the spin accumulation driven by the magnon Edelstein effect including extrinsic contributions [52, 59]. At equilibrium, as shown in Fig. 4(a), the spins at  $\mathbf{k}$  and  $-\mathbf{k}$  points within each magnon band are exactly opposite, resulting in zero net spin. When a temperature gradient is applied, magnons are redistributed from  $\mathbf{k}$  to  $-\mathbf{k}$  (or vice versa, depending band index) under non-equilibrium conditions, generating an excess of magnons with positive spin. Owing to the difference in thermal occupation among bands, the net spin polarization summed over all bands remains nonzero. The calculated response coefficient  $\chi_{zx}$  as a function of temperature is shown in Fig. 4(b), indicating that DMI can induce a sizable polarized spin density. Additionally, the spin distribution depends on the sign of DMI, which enables its reversal through ferroelectric switching. Notably, when the spins lie entirely in the plane, the vertical mirror symmetry of spin space enforces a vanishing  $z$  component Berry curvature, thereby suppressing the magnon Hall effect. Similar spin polarization effects exist in polar layered orthorhombic antiferromagnets, which is presented in the SM [49].

#### D. Material Candidates

Next, we discuss chiral magnons and magnon transport properties in wurtzite-type  $MX$  ( $w-MX$ ), where  $M = \text{Mn, Co}$ ;  $X = \text{O, S, Se}$ . As depicted in Fig. 5(a),  $w-MX$  crystallizes in the polar lattice space group  $P6_3mc$ , where  $M^{2+}$  ions are ferromagnetically aligned within the  $xy$  plane and antiferromagnetically coupled along the  $z$  axis [60, 61]. The vertical mirror symmetry links the opposite-spin sublattices thus preserving the magnons degenerate in the non-relativistic limit. The polar stacking and vertical mirror symmetry enforce uniform DMI vectors between nearest-neighbor  $M^{2+}$  ions within each layer. More importantly, the DMI vectors can be reversed by switching ferroelectric polarization. As shown in Fig. 5(b), the calculated energy barriers between the FE-up and FE-dn states range from 0.08 to 0.35 eV/f.u., while the spontaneous ferroelectric polarization exceeds  $45 \mu\text{C}/\text{cm}^2$  in  $w-MX$ . DFT calculations reveal that  $w\text{-CoS}$  and  $w\text{-CoSe}$  possess easy-axis magnetic anisotropy, whereas  $w\text{-CoO}$ ,  $w\text{-MnS}$ , and  $w\text{-MnSe}$  exhibit easy-plane anisotropy, thereby leading to distinct odd-parity chiral splitting behaviors.

This distinction of magnetic anisotropy can be clearly illustrated by comparing  $w\text{-MnSe}$  and  $w\text{-CoSe}$ . As shown in Figs. 3 and 4, the easy-axis anisotropy in  $w\text{-CoSe}$  stabilizes an  $f$ -wave chiral splitting, whereas the easy-plane anisotropy in  $w\text{-MnSe}$  gives rise to a pronounced fully-gapped odd-parity chiral splitting. Remarkably, despite the sizable  $D_z$ , the weak magnetic anisotropy in

$w$ -MnSe, with  $\mathcal{D}_z = 0.15$  meV and  $\mathcal{K}_x = 0.025$  meV, gives rise to the intriguing Néel vector ( $\hat{\mathcal{N}}$ ) dependence of magnon band splitting and magnon transport. In the following discussion, we define  $\theta$  and  $\phi$  as the angles relative to the  $z$  axis and  $x$  axis, respectively. First, as  $\theta$  varies from zero to  $\pi$ , the magnon gap at  $\Gamma$  and M points exhibits a sinusoidal-like periodic behavior within the LSW approximation, but the gap at K point remains unchanged. A similar periodic behavior occurs in the Edelstein effect, where  $\chi_{zx}$  reaches maximum when  $\theta = \pi/2$ . Conversely, the magnon Hall conductivity  $\kappa_{xy}$  shows a cos-periodic dependence on  $\theta$ , with a maximum at  $\theta = 0$  and a sign reversal at  $\theta = \pi$ . When  $\theta$  is fixed, both  $\kappa_{xy}$  and  $\chi_{xy}$  display isotropic evolutionary features as functions of  $\phi$ , as shown in Figs. 5 (d) and (e).

Beyond the wurtzite-type multiferroics, our symmetry classification further identifies a class of layered orthorhombic antiferromagnetic multiferroics including both bulk and 2D systems, as shown in Tab. 1 and Fig. 5(e). In particular, we identify several material candidates hosting  $p$ -wave and fully-gapped odd-parity chiral magnons. For instance, bulk  $\text{K}_3\text{Cr}_2\text{F}_7$  [62, 63] and monolayer VSBrl [25, 64] exhibit easy-axis A-type antiferromagnetic order accompanied by pronounced chiral magnon splitting, with magnon gap exceeding 5 meV. Notably, all these material candidates are insulating and exhibit both ferroelectric switchability and sizable chiral band splitting, thus providing a solid foundation for future experimental realization.

### III. DISCUSSION

Previous studies have generally suggested that odd-parity magnetism mainly emerges in noncollinear antiferromagnets and is typically accompanied by breaking spin conservation [52, 65, 66]. In this work, however, we find that the intra-sublattice DMI-induced odd-parity chiral magnon band splitting can still preserve spin conservation in easy-axis collinear antiferromagnets. This chiral splitting is analogous to that of chiral magnons driven by Heisenberg exchange interactions in altermagnets [34, 57, 58]. These results indicate that odd-parity chiral magnons with conserved spin do not rely on noncollinear magnetic configurations but can stably exist in collinear antiferromagnetic order, while also exhibiting ferroelectric switchability.

In addition, odd-parity chiral band splitting can induce a variety of intriguing magnon transport phenomena. In particular, easy-axis  $f$ -wave chiral magnons can generate an anomalous Hall effect, whereas easy-plane odd-parity chiral magnons give rise to Edelstein-effect-driven spin accumulation, both responses are reversibly controllable via ferroelectric polarization. Moreover,

owing to the anisotropic nature of the DMI, the system exhibits pronounced Néel-vector-dependent odd-parity chiral splitting and magnon transport. These findings provide a new route for identifying the Néel vector in antiferromagnetic insulators.

In summary, by combining symmetry analysis with LSW calculations, this work establishes a systematic classification of odd-parity chiral magnons in collinear antiferromagnetic multiferroics. Underlying lattice geometry, the resulting chiral splitting can be categorized into planar  $f$ -wave,  $p$ -wave and fully-gapped forms. First-principles calculations reveal a broad family of candidate materials, ranging from bulk to 2D multiferroics, with chiral magnon splitting in  $w$ - $MX$  multiferroics exceeding 10 meV. Notably, in easy-axis antiferromagnetic multiferroics, the intra-sublattice DMI-driven splitting preserves spin angular momentum while exhibiting ferroelectric switchability, in contrast to the odd-parity magnetism in noncollinear antiferromagnets [9, 52, 65, 66]. Overall, our work establishes collinear antiferromagnetic multiferroics as a viable platform for odd-parity chiral magnons and provides new insights into magnetoelectric coupling mechanisms of charge-neutral quasiparticles.

## IV. METHODS

### A. Holstein-Primakoff and Bogoliubov Transformation

The linear spin-wave (LSW) model can be solved using the Holstein-Primakoff (HP) transformation [42]:  $S_{i,\uparrow}^+ \approx \sqrt{2S} \hat{a}_i$ ,  $S_{i,\downarrow}^+ \approx \sqrt{2S} \hat{b}_i^\dagger$ ,  $S_{i,\uparrow}^z = S - \hat{a}_i^\dagger \hat{a}_i$ , and  $S_{i,\downarrow}^z = \hat{b}_i^\dagger \hat{b}_i - S$ . The eigenvalue for the resulting quadratic bosonic Hamiltonian can be solved by a Bogoliubov transformation [43, 44],  $\hat{\mathcal{R}}_{\mathbf{k}}^\dagger \hat{\mathcal{H}}_{\mathbf{k}} \hat{\mathcal{R}}_{\mathbf{k}} = \text{diag}(\epsilon_{\alpha,\mathbf{k}}, \epsilon_{\beta,-\mathbf{k}}, \epsilon_{\alpha,-\mathbf{k}}, \epsilon_{\beta,\mathbf{k}})$ , where  $\hat{\mathcal{R}}_{\mathbf{k}}^\dagger$  and  $\hat{\mathcal{R}}_{\mathbf{k}}$  are  $2 \times 2$  paraunitary matrices, satisfying  $\hat{\mathcal{R}}_{\mathbf{k}}^\dagger \eta \hat{\mathcal{R}}_{\mathbf{k}} = \eta = I_{2 \times 2} \otimes \sigma_z$ . Under the Bogoliubov transformation, the diagonal basis can be expressed as  $\hat{\Psi}_{\mathbf{k}}^\dagger = \hat{\mathcal{R}}_{\mathbf{k}}^\dagger \psi_{\mathbf{k}} = (\hat{\alpha}_{\mathbf{k}}^\dagger, \hat{\beta}_{-\mathbf{k}}, \hat{\alpha}_{-\mathbf{k}}, \hat{\beta}_{\mathbf{k}}^\dagger)$ , whose components represent the eigenmodes. The matrix representing the spin expectation in the  $z$ -direction is  $\Sigma_z = -\sigma_z \otimes I_{2 \times 2}$ , and the corresponding expectation value is given by  $s_z = \hat{\Psi}_{\mathbf{k}}^\dagger \Sigma_z \hat{\Psi}_{\mathbf{k}} / (\hat{\Psi}_{\mathbf{k}}^\dagger \eta \hat{\Psi}_{\mathbf{k}})$ .

### B. Magnon transport

The anomalous thermal Hall conductivity  $\kappa_{xy}$  and magnon Nernst conductivity  $\alpha_{xy}$  are computed by the following formulas  $\kappa_{xy} = \frac{k_B^2 T}{\hbar V} \sum_{n,\mathbf{k}} c_2(\rho) \Omega_n^z(\mathbf{k})$  and  $\alpha_{xy} = \frac{-1}{\hbar V} \sum_{n,\mathbf{k}} S_n^z c_1(\rho) \Omega_n^z(\mathbf{k})$  where  $V$  is the volume, and the weighting functions are defined as  $c_2(\rho) = \int_0^\rho [\log(1 + \rho^{-1})]^2 d\rho$  and  $c_1(\rho) =$

$\int_0^\rho [\log(\rho^{-1} - 1)] d\rho$ . Here  $\rho(\epsilon_{n,\mathbf{k}}) = [\exp(\epsilon_{n,\mathbf{k}}/k_B T) - 1]^{-1}$  is the Bose–Einstein distribution, with  $k_B$  being the Boltzmann constant [56, 67, 68]. The Berry curvature  $\Omega_n^z(\mathbf{k})$  of  $n$ -th band is evaluated for each magnon band and can be computed as  $\Omega_n^z(\mathbf{k}) = \text{Im} \sum_{x,y} \left( \eta \frac{\partial \mathcal{R}_\mathbf{k}}{\partial k_x} \eta \frac{\partial \mathcal{R}_\mathbf{k}}{\partial k_y} \right)_{nn}$ .

The Edelstein coefficient  $\chi_{\mu\nu}$  characterizes the ability of a temperature gradient to induce a spin polarization  $\langle S_\mu \rangle$  in antiferromagnets [52, 59]. In the linear response regime  $\langle S_\mu \rangle = \sum \chi_{\mu\nu} (-\nabla_\nu T)$ ,  $\chi_{\mu\nu}$  can be computed as  $\chi_{\mu\nu} = \frac{1}{VT} \sum_{\mathbf{k}} \sum_{n=1}^N \tau_{n,\mathbf{k}} s_{n,\mathbf{k}}^\mu v_{n,\mathbf{k}}^\nu \epsilon_{n,\mathbf{k}} \frac{\partial \rho(\epsilon_{n,\mathbf{k}})}{\partial \epsilon_{n,\mathbf{k}}}$ , where  $V$  is the volume,  $T$  is the temperature,  $\tau_{n,\mathbf{k}}$  is the relaxation time,  $s_{n,\mathbf{k}}^\mu$  denotes the spin expectation value at  $\mathbf{k}$  points,  $v_{n,\mathbf{k}}^\nu = \frac{1}{\hbar} \frac{\partial \epsilon_{n,\mathbf{k}}}{\partial k_\nu}$  is the group velocity along  $\nu$  direction, and  $\rho(\epsilon_{n,\mathbf{k}})$  is the Bose–Einstein distribution. Here, we assume that the  $\tau$  is independent of both the band index and the wave vector. Note that there is no intrinsic interband contribution to  $\chi_{\mu\nu}$  because it is odd under time-reversal symmetry and therefore vanishes in odd-parity-wave magnets.

### C. DFT calculations

Our DFT calculations are based on the projector augmented wave (PAW) method [69] encoded in the Vienna ab initio simulation package (VASP) [70]. The exchange-correlation function of the Perdew-Becke-Ernzerhof (PBE) [71] form is adopted, and the plane-wave cutoff energy is set to 500 eV. To properly describe the strong electron correlation in the 3d states, the GGA plus on-site repulsion  $U$  method (GGA+ $U$ ) is employed [72]. The effective  $U$  value ( $U_{eff} = U - J$ ) is set to 4 eV for Mn and Co, and 2.5 eV is set for V. The main results will not change if other reasonable values are adopted. The structural optimizations are carried out until the forces acting on atoms are smaller than 0.001 eV/Å. The ferroelectric polarization is calculated by the Berry phase method [73]. The spin exchange parameters are calculated by the four states mapping method [74, 75]. The ferroelectric energy barrier are calculated by the climbing image nudged elastic band (CI-NEB) method [76].

### ACKNOWLEDGMENT

The authors thank Prof. Bo Li for helpful discussions. This work is supported by the National Natural Science Foundation of China (Grant No. 12374092 and No. T2425029), Natural Science Basic Research Program of Shaanxi (Program No. 2023-JC-YB-017), Shaanxi Fundamental Science Research Project for Mathematics and Physics (Grant No. 22JSQ013), “Young Talent Support Plan”

of Xi'an Jiaotong University, and the Xiaomi Young Talents Program.

---

- [1] V. Baltz, A. Manchon, M. Tsoi, T. Moriyama, T. Ono, and Y. Tserkovnyak, Antiferromagnetic spintronics, *Rev. Mod. Phys.* **90**, 015005 (2018).
- [2] R. Ramesh and N. A. Spaldin, Multiferroics: progress and prospects in thin films, *Nat. Mater.* **6**, 21 (2007).
- [3] M. Fiebig, T. Lottermoser, D. Meier, and M. Trassin, The evolution of multiferroics, *Nat. Rev. Mater.* **1**, 16046 (2016).
- [4] H. Schmid, Multi-ferroic magnetoelectrics, *Ferroelectrics* **162**, 317 (1994).
- [5] N. A. Spaldin, S.-W. Cheong, and R. Ramesh, Multiferroics: Past, present, and future, *Phys. Today* **63**, 38 (2010).
- [6] C. Xu, P. Chen, H. Tan, Y. Yang, H. Xiang, and L. Bellaiche, Electric-field switching of magnetic topological charge in type-I multiferroics, *Phys. Rev. Lett.* **125**, 037203 (2020).
- [7] B. B. Van Aken, T. T. M. Palstra, A. Filippetti, and N. A. Spaldin, The origin of ferroelectricity in magnetoelectric  $\text{YMnO}_3$ , *Nat. Mater.* **3**, 164 (2004).
- [8] T. Kimura, T. Goto, H. Shintani, K. Ishizaka, T. Arima, and Y. Tokura, Magnetic control of ferroelectric polarization, *Nature* **426**, 55 (2003).
- [9] Q. Song, C. A. Occhialini, E. Ergeçen, B. Ilyas, D. Amoroso, P. Barone, J. Kapeghian, K. Watanabe, T. Taniguchi, A. S. Botana, S. Picozzi, N. Gedik, and R. Comin, Evidence for a single-layer van der Waals multiferroic, *Nature* **602**, 601 (2022).
- [10] L. Ponet, S. Artyukhin, T. Kain, J. Wettstein, A. Pimenov, A. Shuvaev, X. Wang, S.-W. Cheong, M. Mostovoy, and A. Pimenov, Topologically protected magnetoelectric switching in a multiferroic, *Nature* **607**, 81 (2022).
- [11] S. Dong, H. Xiang, and E. Dagotto, Magnetoelectricity in multiferroics: a theoretical perspective, *Nat. Sci. Rev.* **6**, 629 (2019).
- [12] J. Wang, J. B. Neaton, H. Zheng, V. Nagarajan, S. B. Ogale, B. Liu, D. Viehland, V. Vaithyanathan, D. G. Schlom, U. V. Waghmare, N. A. Spaldin, K. M. Rabe, M. Wuttig, and R. Ramesh, Epitaxial  $\text{BiFeO}_3$  multiferroic thin film heterostructures, *Science* **299**, 1719 (2003).
- [13] J. Y. Ni, P. S. Wang, J. L. Lu, and H. J. Xiang, Realizing magnetoelectric coupling with hydrogen intercalation, *Phys. Rev. Lett.* **122**, 117601 (2019).

- [14] A. Malashevich and D. Vanderbilt, First principles study of improper ferroelectricity in  $\text{TbMnO}_3$ , [Phys. Rev. Lett. \*\*101\*\*, 037210 \(2008\)](#).
- [15] H. J. Xiang, S.-H. Wei, M.-H. Whangbo, and J. L. F. Da Silva, Spin-orbit coupling and ion displacements in multiferroic  $\text{TbMnO}_3$ , [Phys. Rev. Lett. \*\*101\*\*, 037209 \(2008\)](#).
- [16] L. Šmejkal, J. Sinova, and T. Jungwirth, Beyond conventional ferromagnetism and antiferromagnetism: A phase with nonrelativistic spin and crystal rotation symmetry, [Phys. Rev. X \*\*12\*\*, 031042 \(2022\)](#).
- [17] L. Šmejkal, J. Sinova, and T. Jungwirth, Emerging research landscape of altermagnetism, [Phys. Rev. X \*\*12\*\*, 040501 \(2022\)](#).
- [18] S. Hayami, H. Kusunose, and Y. Motome, Asymmetric magnon excitation by spontaneous toroidal ordering, [J. Phys. Soc. Jpn. \*\*85\*\*, 053705 \(2016\)](#).
- [19] Y. Liu, J. Yu, and C.-C. Liu, Twisted magnetic van der Waals bilayers: An ideal platform for altermagnetism, [Phys. Rev. Lett. \*\*133\*\*, 206702 \(2024\)](#).
- [20] R. He, D. Wang, N. Luo, J. Zeng, K.-Q. Chen, and L.-M. Tang, Nonrelativistic spin-momentum coupling in antiferromagnetic twisted bilayers, [Phys. Rev. Lett. \*\*130\*\*, 046401 \(2023\)](#).
- [21] X. Duan, J. Zhang, Z. Zhu, Y. Liu, Z. Zhang, I. Žutić, and T. Zhou, Antiferroelectric altermagnets: Antiferroelectricity alters magnets, [Phys. Rev. Lett. \*\*134\*\*, 106801 \(2025\)](#).
- [22] M. Gu, Y. Liu, H. Zhu, K. Yananose, X. Chen, Y. Hu, A. Stroppa, and Q. Liu, Ferroelectric switchable altermagnetism, [Phys. Rev. Lett. \*\*134\*\*, 106802 \(2025\)](#).
- [23] W. Zhao, X. Zhou, Z. Guo, T. Zhu, J. Chen, H. Li, Z. Cheng, X. Wang, and W. Wang, Multiferroic phase transition between multiple types of collinear compensated magnets, [Nat. Commun. \(2026\)](#).
- [24] W. Sun, C. Yang, X. Wang, S. Huang, and Z. Cheng, Altermagnetic multiferroics with symmetry-locked magnetoelectric coupling, [Nat. Mater. \(2026\)](#).
- [25] Z. Zhu, X. Duan, J. Zhang, B. Hao, I. Zutic, and T. Zhou, Two-dimensional ferroelectric altermagnets: From model to material realization, [Nano Lett. \*\*25\*\*, 9456 \(2025\)](#).
- [26] S. Wang, W.-W. Wang, J. Fan, X. Zhou, X.-P. Li, and L. Wang, Two-dimensional dual-switchable ferroelectric altermagnets: altering electrons and magnons, [Nano Lett. \*\*25\*\*, 14618 \(2025\)](#).
- [27] X. Chen, J. Ren, Y. Zhu, Y. Yu, A. Zhang, P. Liu, J. Li, Y. Liu, C. Li, and Q. Liu, Enumeration and representation theory of spin space groups, [Phys. Rev. X \*\*14\*\*, 031038 \(2024\)](#).
- [28] Y. Jiang, Z. Song, T. Zhu, Z. Fang, H. Weng, Z.-X. Liu, J. Yang, and C. Fang, Enumeration of spin-space groups: Toward a complete description of symmetries of magnetic orders, [Phys. Rev. X \*\*14\*\*, 031039 \(2024\)](#).

- [29] Z. Xiao, J. Zhao, Y. Li, R. Shindou, and Z.-D. Song, Spin space groups: Full classification and applications, *Phys. Rev. X* **14**, 031037 (2024).
- [30] Q. N. Meier, A. Carta, C. Ederer, and A. Cano, Net and compensated altermagnetism from staggered orbital order: Layer-dependent spin splitting in  $\text{Sr}_{n+1}\text{Cr}_n\text{O}_{3n+1}$ , *Phys. Rev. Lett.* **136**, 116705 (2026).
- [31] I. I. Mazin, How to define and calculate the degree of spin polarization in ferromagnets, *Phys. Rev. Lett.* **83**, 1427 (1999).
- [32] J. Berakdar, Probing the spin polarization in ferromagnets, *Phys. Rev. Lett.* **83**, 5150 (1999).
- [33] A. V. Chumak, V. I. Vasyuchka, A. A. Serga, and B. Hillebrands, Magnon spintronics, *Nat. Phys.* **11**, 453 (2015).
- [34] L. Šmejkal, A. Marmodoro, K.-H. Ahn, R. González-Hernández, I. Turek, S. Mankovsky, H. Ebert, S. W. D'Souza, O. Šipr, J. Sinova, and T. Jungwirth, Chiral magnons in altermagnetic  $\text{RuO}_2$ , *Phys. Rev. Lett.* **131**, 256703 (2023).
- [35] I. Dzyaloshinsky, A thermodynamic theory of “weak” ferromagnetism of antiferromagnetics, *J. Phys. Chem. Solids* **4**, 241 (1958).
- [36] T. Moriya, Anisotropic superexchange interaction and weak ferromagnetism, *Phys. Rev.* **120**, 91 (1960).
- [37] J. Ni, Y. Jin, Q. Du, and G. Chang, Magnon nonlinear Hall effect in two-dimensional antiferromagnetic insulators, *Phys. Rev. B* **112**, 054424 (2025).
- [38] R. Cheng, S. Okamoto, and D. Xiao, Spin Nernst effect of magnons in collinear antiferromagnets, *Phys. Rev. Lett.* **117**, 217202 (2016).
- [39] V. A. Zyuzin and A. A. Kovalev, Magnon spin Nernst effect in antiferromagnets, *Phys. Rev. Lett.* **117**, 217203 (2016).
- [40] L. Bai, R.-W. Zhang, W. Feng, and Y. Yao, Anomalous Hall effect in type IV 2D collinear magnets, *Phys. Rev. Lett.* **135**, 036702 (2025).
- [41] Y. Liu, S.-D. Guo, Y. Li, and C.-C. Liu, Two-dimensional fully compensated ferrimagnetism, *Phys. Rev. Lett.* **134**, 116703 (2025).
- [42] T. Holstein and H. Primakoff, Field dependence of the intrinsic domain magnetization of a ferromagnet, *Phys. Rev.* **58**, 1098 (1940).
- [43] N. N. Bogoljubov, V. V. Tolmachov, and D. V. Širkov, A new method in the theory of superconductivity, *Fortschr. Phys.* **6**, 605 (1958).
- [44] J. G. Valatin, Comments on the theory of superconductivity, *Nuovo. Cim.* **7**, 843 (1958).

- [45] Q. Du, Z. Zhang, J. Ni, Z. Jiang, and L. Bellaiche, Nonreciprocal magnons in layered antiferromagnets  $\text{VPX}_3$  ( $X = \text{S, Se, Te}$ ), *Phys. Rev. B* **112**, L100408 (2025).
- [46] T. Matsumoto and S. Hayami, Nonreciprocal magnons due to symmetric anisotropic exchange interaction in honeycomb antiferromagnets, *Phys. Rev. B* **101**, 224419 (2020).
- [47] T. J. Sato and K. Matan, Nonreciprocal magnons in noncentrosymmetric magnets, *J. Phys. Soc. Jpn.* **88**, 081007 (2019).
- [48] G. Gitgeatpong, Y. Zhao, P. Piyawongwatthana, Y. Qiu, L. W. Harriger, N. P. Butch, T. J. Sato, and K. Matan, Nonreciprocal magnons and symmetry-breaking in the noncentrosymmetric antiferromagnet, *Phys. Rev. Lett.* **119**, 047201 (2017).
- [49] See Supplemental Material at ... for (i) the derivation of the Berry curvature and (ii) the results of the DFT calculations and bilayer fully antiferromagnets.
- [50] M. Kawano, Y. Onose, and C. Hotta, Designing Rashba–Dresselhaus effect in magnetic insulators, *Commun. Phys.* **2**, 27 (2019).
- [51] N. Okuma, Magnon spin-momentum locking: Various spin vortices and Dirac magnons in noncollinear antiferromagnets, *Phys. Rev. Lett.* **119**, 107205 (2017).
- [52] R. R. Neumann, R. Jaeschke-Ubiergo, R. Zarzuela, L. Šmejkal, J. Sinova, and A. Mook, Odd-parity-wave magnons and nonrelativistic thermal Edelstein effect, [preprint arXiv:2603.05415](#) (2026).
- [53] D. Xiao, M. C. Chang, and Q. Niu, Berry phase effects on electronic properties, *Rev. Mod. Phys.* **82**, 1959 (2010).
- [54] W. F. Brinkman and R. J. Elliott, Theory of spin-space groups, *Proc. R. Soc. A* **294**, 343 (1966).
- [55] R. Matsumoto and S. Murakami, Theoretical prediction of a rotating magnon wave packet in ferromagnets, *Phys. Rev. Lett.* **106**, 197202 (2011).
- [56] Y. Onose, T. Ideue, H. Katsura, Y. Shiomi, N. Nagaosa, and Y. Tokura, Observation of the magnon Hall effect, *Science* **329**, 297 (2010).
- [57] Q. Cui, B. Zeng, P. Cui, T. Yu, and H. Yang, Efficient spin Seebeck and spin Nernst effects of magnons in altermagnets, *Phys. Rev. B* **108**, L180401 (2023).
- [58] K. Wu, J. Dong, M. Zhu, F. Zheng, and J. Zhang, Magnon splitting and magnon spin transport in altermagnets, *Chin. Phys. Lett.* **42**, 070702 (2025).
- [59] B. Li, A. Mook, A. Raeliarijaona, and A. A. Kovalev, Magnonic analog of the Edelstein effect in antiferromagnetic insulators, *Phys. Rev. B* **101**, 024427 (2020).

- [60] M. J. Grzybowski, C. Autieri, J. Domagala, C. Krasucki, A. Kaleta, S. Kret, K. Gas, M. Sawicki, R. Bożek, J. Suffczyński, and W. Pacuski, Wurtzite vs. rock-salt MnSe epitaxy: electronic and altermagnetic properties, [Nanoscale](#) **16**, 6259 (2024).
- [61] D. Bezzega, I. Khan, and J. Hong, High performance room temperature multiferroic properties of *w*-MnSe altermagnet, [Adv. Funct. Mater.](#) **35**, 2505813 (2025).
- [62] Y. Zhou, H.-M. Zhang, C.-A. Ji, H. Xiang, S. Dong, J. M. Rondinelli, and X.-Z. Lu, Piezomagnetism-driven magnetoelectric coupling in altermagnetic multiferroic  $K_3Cr_2F_7$ , [Phys. Rev. B](#) **112**, 094412 (2025).
- [63] K. Xu, X.-Z. Lu, and H. Xiang, Designing new ferroelectrics with a general strategy, [npj Quant. Mater.](#) **2**, 1 (2017).
- [64] H. Tan, M. Li, H. Liu, Z. Liu, Y. Li, and W. Duan, Two-dimensional ferromagnetic-ferroelectric multiferroics in violation of the  $d^0$  rule, [Phys. Rev. B](#) **99**, 195434 (2019).
- [65] Q. Song, S. Stavrić, P. Barone, A. Droghetti, D. S. Antonenko, J. W. Venderbos, C. A. Occhialini, B. Ilyas, E. Ergeçen, N. Gedik, S.-W. Cheong, R. M. Fernandes, S. Picozzi, and R. Comin, Electrical switching of a *p*-wave magnet, [Nature](#) **642**, 64 (2025).
- [66] J. Priessnitz, A. B. Hellenes, R. Comin, and L. Šmejkal, Ferroelectric *p*-wave magnets, [preprint arXiv:2603.19107](#) (2026).
- [67] R. Matsumoto, R. Shindou, and S. Murakami, Thermal Hall effect of magnons in magnets with dipolar interaction, [Phys. Rev. B](#) **89**, 054420 (2014).
- [68] H. Katsura, N. Nagaosa, and P. A. Lee, Theory of the thermal Hall effect in quantum magnets, [Phys. Rev. Lett.](#) **104**, 066403 (2010).
- [69] P. E. Blöchl, Projector augmented-wave method, [Phys. Rev. B](#) **50**, 17953 (1994).
- [70] G. Kresse and J. Furthmüller, Efficiency of ab-initio total energy calculations for metals and semiconductors using a plane-wave basis set, [Comp. Mater. Sci.](#) **6**, 15 (1996).
- [71] J. P. Perdew, K. Burke, and M. Ernzerhof, Generalized gradient approximation made simple, [Phys. Rev. Lett.](#) **77**, 3865 (1996).
- [72] A. I. Liechtenstein, V. I. Anisimov, and J. Zaanen, Density-functional theory and strong interactions: Orbital ordering in Mott-Hubbard insulators, [Phys. Rev. B](#) **52**, R5467 (1995).
- [73] R. D. King-Smith and D. Vanderbilt, Theory of polarization of crystalline solids, [Phys. Rev. B](#) **47**, 1651(R) (1993).

- [74] H. J. Xiang, E. J. Kan, S.-H. Wei, M.-H. Whangbo, and X. G. Gong, Predicting the spin-lattice order of frustrated systems from first principles, *Phys. Rev. B* **84**, 224429 (2011).
- [75] H. Xiang, C. Lee, H.-J. Koo, X. Gong, and M.-H. Whangbo, Magnetic properties and energy-mapping analysis, *Dalton Trans.* **42**, 823 (2013).
- [76] G. Henkelman, B. P. Uberuaga, and H. Jónsson, A climbing image nudged elastic band method for finding saddle points and minimum energy paths, *J. Chem. Phys.* **113**, 9901 (2000).

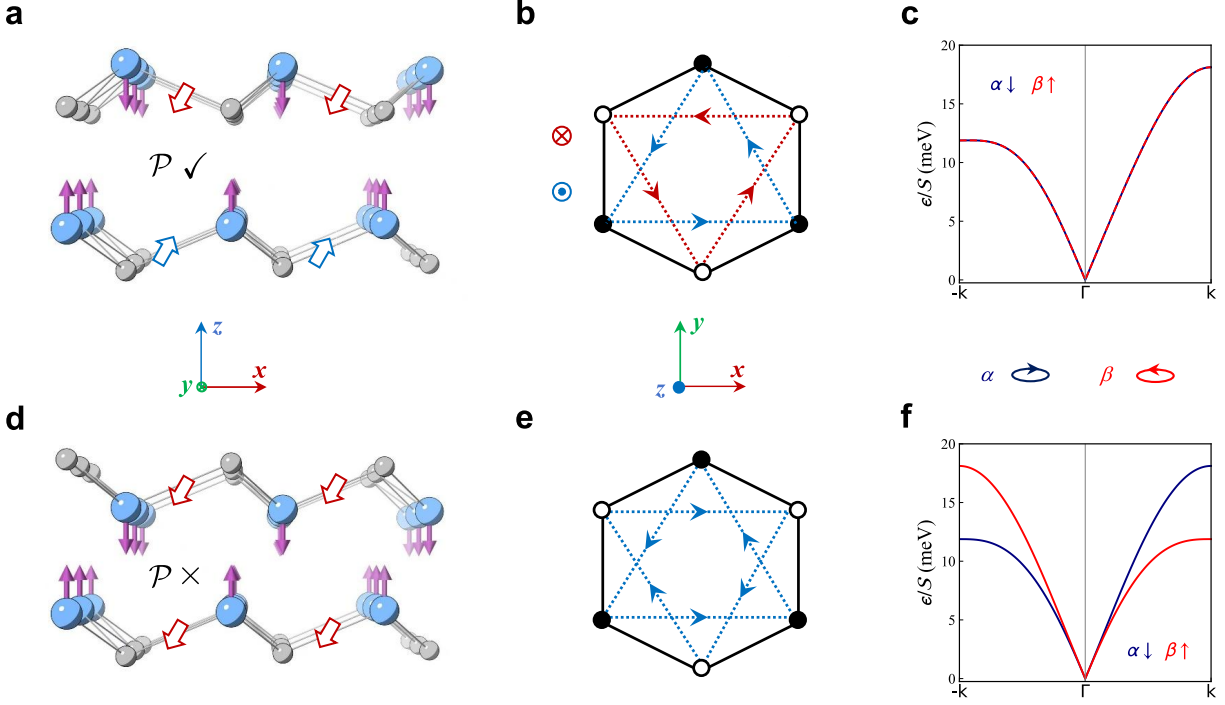


FIG. 1. Realizing odd-parity chiral magnons in layered antiferromagnets. Side view of bilayer antiferromagnets with  $\mathcal{P}$  preserved (a) and  $\mathcal{P}$  broken (d), where blue balls refer to the magnetic ions. Top view of bilayer antiferromagnets with  $\mathcal{P}$  preserved (b) and  $\mathcal{P}$  broken (e). White and black circles represent up and down spins, respectively. The direction of DMI is indicated by  $\odot$  and  $\otimes$ . The magnon bands for bilayer antiferromagnets with  $\mathcal{P}$  preserved (c) and with  $\mathcal{P}$  broken (f).

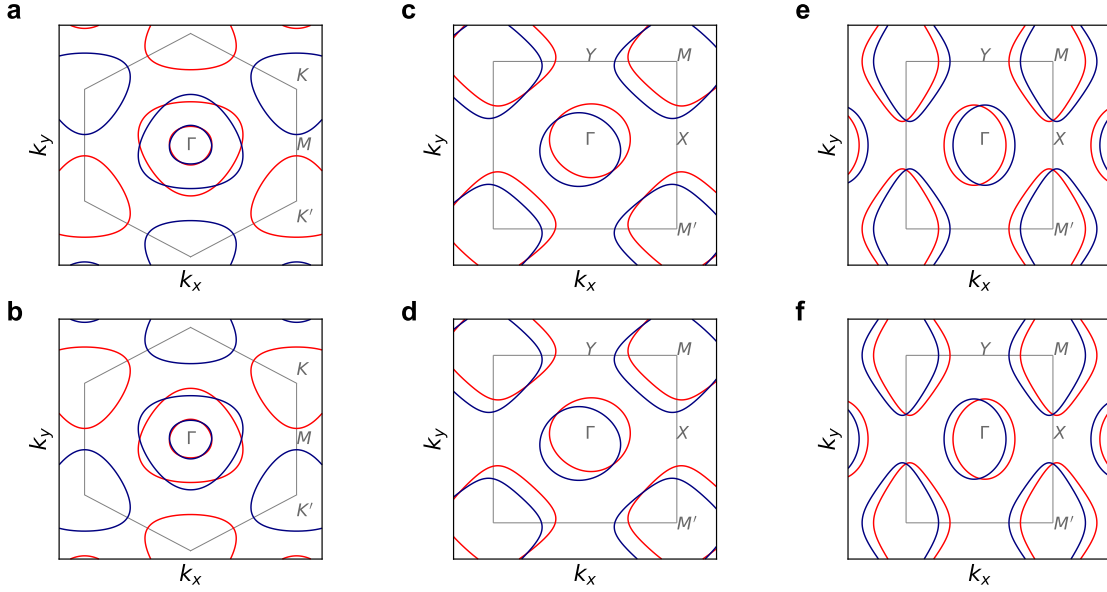


FIG. 2. The isoenergy surfaces for odd-parity chiral magnon bands at  $\mathbf{k}_z = 0$ , where the red and blue lines represent modes with  $s_z = \pm 1$ . (a)  $f$ -wave chiral magnons for layered hexagonal antiferromagnets. (c)  $p$ -wave chiral magnons for layered square antiferromagnets. (e)  $p$ -wave chiral magnons for layered rectangular antiferromagnets. (b), (d) and (f) are the magnon bands with reversing the sign of DMI.

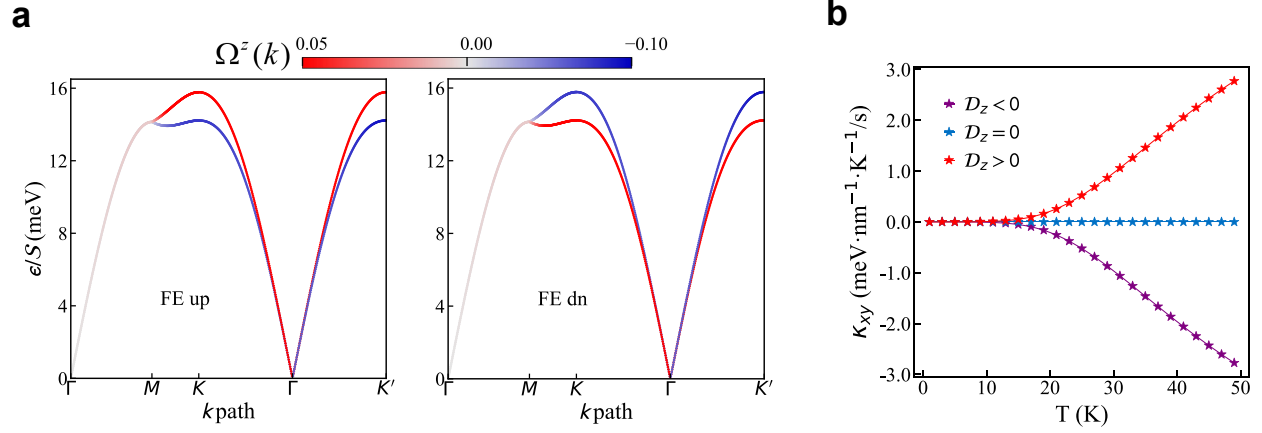


FIG. 3. Easy-axis  $f$ -wave chiral magnons and ferroelectric switching. (a) Magnon bands weighted by the  $z$  component Berry curvature for different ferroelectric states. (b) The calculated magnon Hall conductivity  $\kappa_{xy}$  with different  $D_z$ . Here,  $\mathcal{J}_1 = 5$  meV and  $D_z = 0.15$  meV (left) and  $D_z = -0.15$  meV (right).

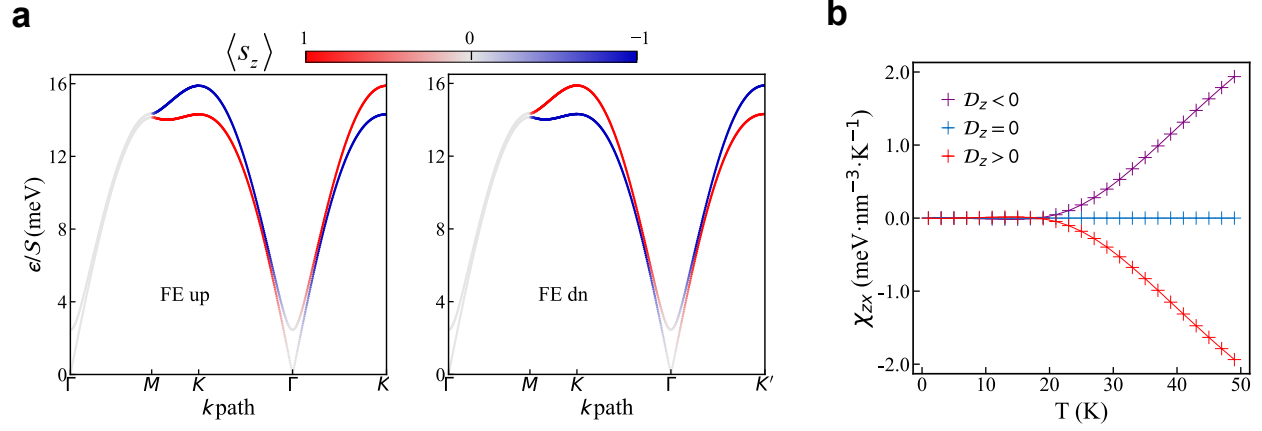


FIG. 4. Easy-plane magnons and ferroelectric switching. (a) The magnon bands weighted by the  $\langle S^z \rangle$  in easy-plane antiferromagnetic lattice for different ferroelectric states. (b) The calculated Edelstein response parameter  $\chi_{zx}$  with different  $D_z$ . The spin parameters are adopted from the  $w$ -MnSe with  $\mathcal{K}_x = 0.05$  meV.

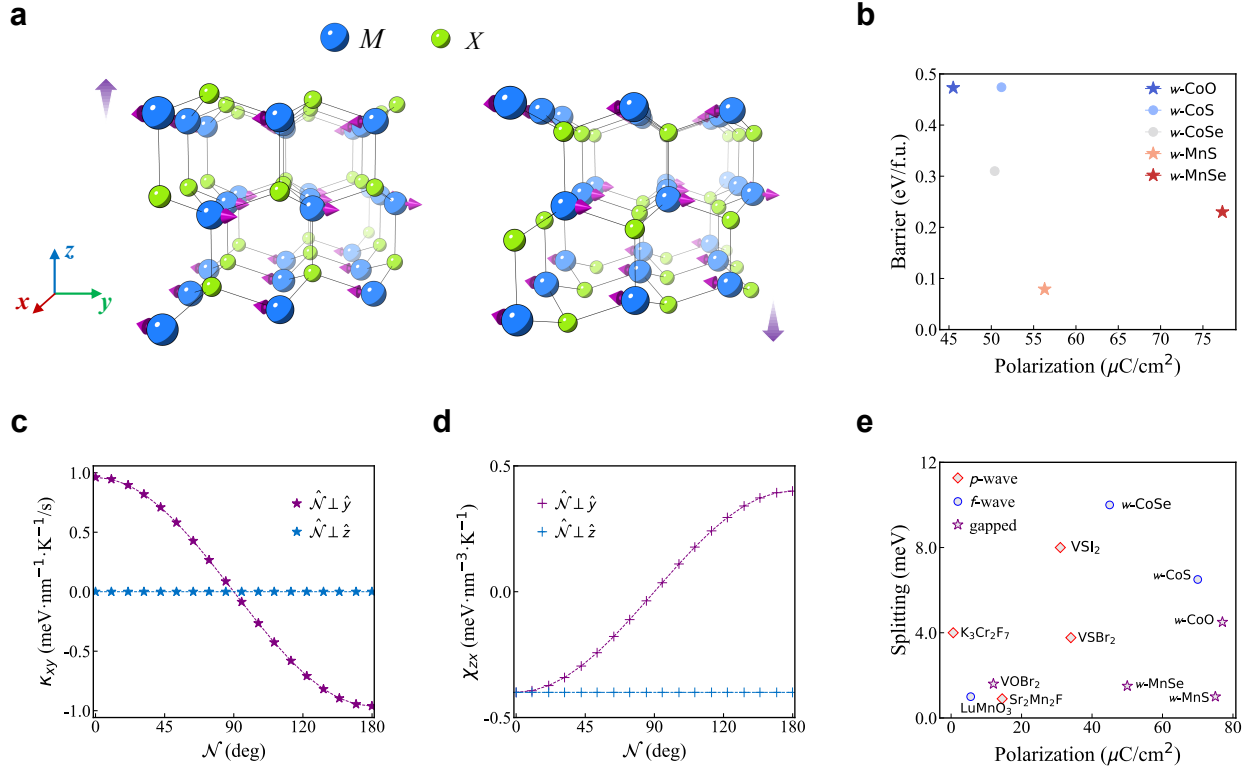


FIG. 5. Odd-parity chiral magnon splitting in material candidates. (a) Crystal and magnetic structure of  $w-MX$ . (b) The calculated ferroelectric energy barriers and polarization of  $w-MX$ . (c) The  $\hat{\mathcal{N}}$  dependent Magnon Hall conductivity  $\kappa_{xy}$ . (d) Edelstein effect coefficient  $\chi_{zx}$  in  $w\text{-MnSe}$ . (e) Calculated ferroelectric polarization and the maximum magnon band splitting for the  $w-MX$  and orthorhombic layered antiferromagnets.